APPLIED PHYSICS

Powering up perovskite photoresponse

Low-dimensional perovskites could help enhance solar cell performance

By **Osman M. Bakr** *and* **Omar F. Mohammed**

The most notable scientific milestone in photovoltaics in the past several years is the emergence of solar cells based on hybrid organic-inorganic perovskite materials. While conventional silicon and thin-film solar cells have seen steady improvements in their power-conversion efficiencies (PCEs) spanning several decades, hybrid perovskite solar cells have already reached a certified 22.1% PCE (*1*), matching conventional solar cell technologies in only a few years since their first device architecture was tested. Setting the stage for a disruptive technology in the field of photovoltaics is the seemingly winning combination of properties of hybrid perovskite materials: high absorption coefficient and a tunable energy band gap in wavelengths ideal for solar cells; long diffusion lengths and lifetimes for photogenerated charge carriers, which easily dissociate into efficiently collected electrons and holes; Earth-abundant elemental composition; and their compatibility with low-cost and low-temperature fabrication methods *(2–5)*. On page 1288 of this issue, Blancon *et al.* (*6*) report on the observation of an enhanced photoresponse for layered perovskite materials. The results add, literally, a new dimension to the further development of high-performance perovskite solar cells.

There are crucial factors debilitating hybrid perovskite materials in solar cells. A variety of causes contribute to their instability, including moisture and light-induced degradation; defective surface structure; and ion migration under operating conditions (*7, 8*). In essence, hybrid perovskites are ionic salts, readily soluble in polar solvents, with the unit cell formula AMX_3 (X is a halogen, M is a metal that can coordinate to six halides, and A is a small organic or inorganic cation). The perovskite structure is a three-dimensional (3D) network of corner-sharing $[MX_6]^-$ octahedra, balanced with an equal number of positively charged cations residing within the small cavity spaces left behind by the metal halide network (see the figure). The geometric restriction imposed by the size of the cavity limits the choice of A-site species to a small set of cations such as methylammonium (MA), formamidinium (FA), or Cs; and the M-site to Pb, Sn, or Ge. Of the latter group of elements, Pb-based perovskites are the most stable. These geometric constraints for 3D perovskites have made it difficult to find materials within this family of compounds that are both stable and possess the optoelectronic characteristics demanded by solar cell applications.

Substituting the small A-site cation, either partially or completely, with organic cations larger than the perovskite network cavities leads to the breakup of this metal halide network into sheets, rods, or clusters, spatially separated by sublattices of the large cations. Such compounds are often referred to as reduced-dimensionality or low-dimensional (2D for sheets, 1D for rods, and 0D for isolated clusters) perovskite derivatives (*9–12*). Owing to the large number of possible cations compared to the 3D counterpart, the potential set of such compounds is practically enumerable. Moreover, the flexibility offered by the unrestricted size of the organic cation allows for freedom to tailor the properties of the materials (through the appropriate use of functional organic molecules) such that they are made intrinsically more robust against the degradation factors affecting 3D perovskites. Furthermore, the relaxed geometric requirements in low-dimensional perovskites offer additional paths for designing perovskites with more environmentally benign elements than Pb, but without compromising performance.

Despite these advantages, the large exciton binding energy and quantum confinement induced by the low dimensionality and layered nature of these compounds implies that they are inherently excitonic materials, in which the photogenerated electron-hole pairs are strongly bound and thus tend to recombine before they can separate into free charges and be collected. The prevailing wisdom is that these reduced-dimensionality perovskites are potentially useful for light-emitting applications, but are inefficient for solar cells and photodetectors, for which efficient electron-hole separation is a prerequisite. The results of Blancon *et al.* might change this widely accepted view.

Blancon *et al.* reinvestigated a type of reduced-dimensionality perovskite known as Ruddlesden-Popper–type 2D perovskites. In these 2D structures, the $[PbI_6]^-$ octahedra are arranged in equal-thickness sheets periodically separated by large *n*-butylammonium (BA) cations (see the

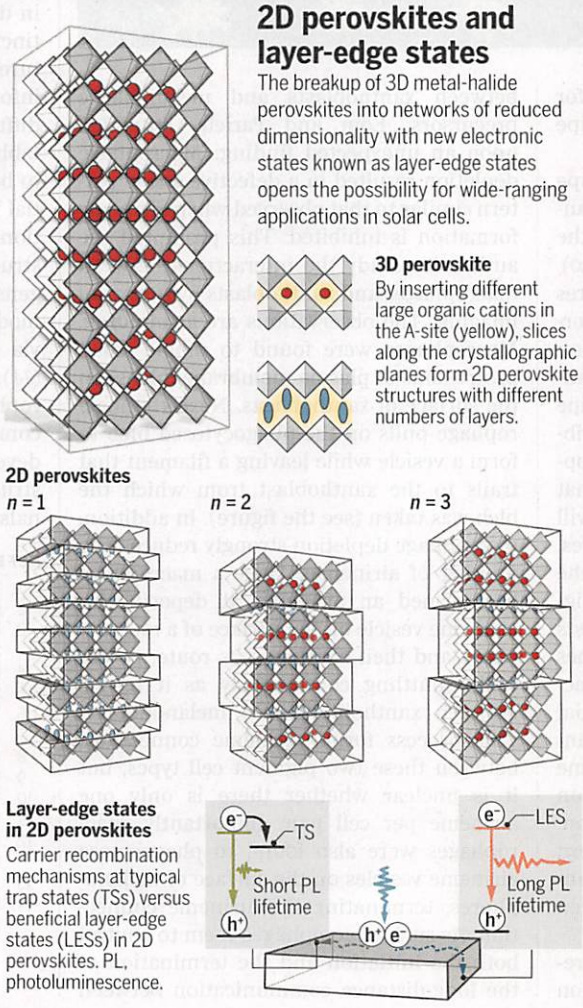

GRAPHIC: V. ALTOUNIAN/*SCIENCE*

King Abdullah University of Science and Technology (KAUST), KAUST Solar Center (KSC), Division of Physical Sciences and Engineering (PSE), Thuwal 23955-6900, Kingdom of Saudi Arabia. Email: osman.bakr@kaust.edu.sa; omar.abdelsaboor@kaust.edu.sa

Macrophages orchestrate stripe development in zebrafish

Stripes are formed by pigmented melanophores (black) that alternate with yellow xanthophores in the interstripe region.

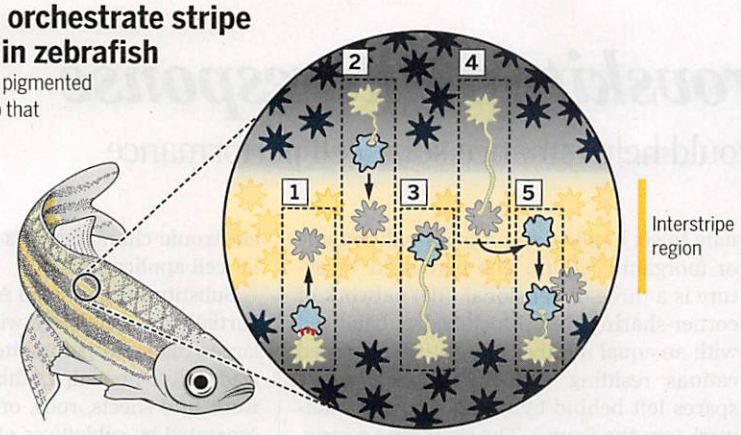

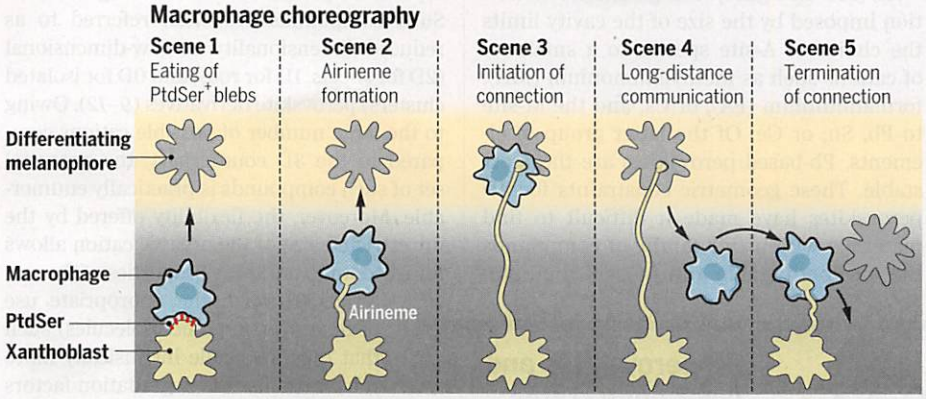

GRAPHIC: ADAPTED BY K. SUTLIFF/*SCIENCE*

another unexpected tissue-specific role for macrophages—the orchestration of stripe development in zebrafish.

Dark-pigmented melanophores (stripe region) alternate with yellow-colored xanthophores (interstripe region) to form the zebra pattern on zebrafish (see the photo). To achieve this pattern, melanophores and xanthophores need to be spatially organized. Long-distance communication between melanophore precursors and xanthophore precursors is essential for stripe development. Both cell types are distributed broadly on the flank of the developing zebrafish. Xanthophore precursors that populate the future interstripe region will differentiate into yellow xanthophores, whereas xanthophore precursors in the future stripe regions will remain as unpigmented xanthoblasts. These xanthoblasts extend long projections called airinemes to melanophore precursors. This interaction appears to be essential for the spatial organization of melanophores because xanthoblast depletion or blockage of airineme generation results in the mislocalization of melanophores in the interstripe region. The end result is a defective zebra pattern (*12*). The precise molecular mechanisms underlying airineme communication between pigment cells remain unknown.

In studying the cellular mechanisms required for long-distance communication between xanthoblasts and melanophore precursors, Eom and Parichy stumbled upon an unexpected finding: Macrophage depletion resulted in a defective stripe pattern similar to that observed when airineme formation is inhibited. This prompted the authors to study the interactions between macrophages and xanthoblasts by intravital imaging. The observations are astounding. Macrophages were found to nibble small protrusions of plasma membrane (blebs) on the surface of xanthoblasts. Next, the macrophage pulls on the phagocytosed bleb to form a vesicle while leaving a filament that trails to the xanthoblast from which the bleb was taken (see the figure). In addition, macrophage depletion strongly reduced the number of airinemes. Once a macrophage has formed an airineme, it deposits the airineme vesicle on the surface of a melanophore and then continues its route, potentially shuttling continuously as it ferries between xanthoblasts and melanophores. This process forms airineme connections between these two pigment cell types, but it is unclear whether there is only one airineme per cell pair. Importantly, macrophages were also found to phagocytose airineme vesicles on the surface of melanophores, terminating the airineme connection. As such, macrophages seem to control both the initiation and the termination of the long-distance communication between melanophores and xanthoblasts, which suggests that these cells are central organizers of stripe development in zebrafish.

How do macrophages recognize the blebs on xanthoblasts? Eom and Parichy determined that the PtdSer signal is highly expressed on xanthoblast blebs. Blockade of PtdSer generation was sufficient to reduce the number of airinemes. Macrophages express many different receptors for PtdSer, including Mer tyrosine kinase (MerTK). MerTK is highly expressed on macrophages from multiple mouse tissues (*4*), is expressed on human macrophages (*13*), and is conserved in chimpanzee, dog, cow, rat, chicken, frog, and zebrafish. What better bait than PtdSer to tempt macrophages to engulf the bleb on xanthoblasts and initiate airineme formation? That nature would select this ancient and widely conserved macrophage eat-me signal for the long-distance communication between different nonimmune cells is particularly appealing. Are macrophages also orchestrating similar intercellular communication systems in other tissues and species?

Spatial patterning also takes place during embryonic morphogenesis. Precursor cells in different locations differentiate into distinct subsets of cells to form complex structures, but how do cells obtain the spatial information that determines their fate? The diffusion of soluble morphogens, which establish concentration gradients, is proposed to be a main mechanism for providing spatial information to cells. But in many situations, diffusion may be blocked by cellular structures. Active transport of morphogens has been proposed as an alternative model. Morphogens also can be transported via cellular protrusions called cytonemes (*14*). It is tempting to speculate that macrophages could function in long-distance communication between cells of different developmental zones through airineme-like structures that would carry morphogen signals and orchestrate organ development. ■

REFERENCES

1. D. S. Eom, D. M. Parichy, *Science* **355**, 1317 (2017).
2. O. Takeuchi, S. Akira, *Cell* **140**, 805 (2010).
3. K. K. Penberthy, K. S. Ravichandran, *Immunol. Rev.* **269**, 44 (2016).
4. E. L. Gautier *et al.*, *Nat. Immunol.* **13**, 1118 (2012).
5. F. Ginhoux, S. Jung, *Nat. Rev. Immunol.* **14**, 392 (2014).
6. Y. Okabe, R. Medzhitov, *Nat. Immunol.* **17**, 9 (2016).
7. R. C. Paolicelli *et al.*, *Science* **333**, 1456 (2011).
8. A. E. Grigoriadis *et al.*, *Science* **266**, 443 (1994).
9. M. Haldar *et al.*, *Cell* **156**, 1223 (2014).
10. I. Theurl *et al.*, *Nat. Med.* **22**, 945 (2016).
11. M. Guilliams *et al.*, *J. Exp. Med.* **210**, 1977 (2013).
12. D. S. Eom, E. J. Bain, L. B. Patterson, M. E. Grout, D. M. Parichy, *eLife* **4**, e12401 (2015).
13. J. Xue *et al.*, *Immunity* **40**, 274 (2014).
14. M. Buszczak, M. Inaba, Y. M. Yamashita, *Trends Cell Biol.* **26**, 526 (2016).

10.1126/science.aam9743

detected in absorption is co-rotating in an extended disk. Most simulations predict precisely such an extended planar configuration fed by cold flows (*31*), with properties similar to those observed in the $z = 4.26$ DLA (*32*). The DLA toward SDSS J120110.31+211758.5 is harder to classify because its absorption is seen over the full velocity range of the emission profile, which spans almost 500 km s^{-1}. This is more indicative of a large-scale outflow or a highly perturbed system, which is corroborated by the spatial shift in the [C II] 158-μm line emission (fig. S2). In both cases, it is clear that the DLA host galaxy has effectively enriched its inner gaseous halo, in agreement with recent simulations (*33*).

Our results indicate that the galaxies giving rise to high-metallicity DLAs have characteristics similar to the high-mass end of the LBG population (*9*, *30*) and are embedded in a large reservoir of neutral H I gas. This gas is being enriched by the galaxy but is bound to it, as there is almost no systematic velocity offset between the metals seen in absorption and the [C II] 158-μm line in emission. This observation suggests that this halo gas will eventually accrete back onto the galaxy, providing enriched gas for future star formation.

REFERENCES AND NOTES

1. J. X. Prochaska, S. Herbert-Fort, A. M. Wolfe, *Astrophys. J.* **635**, 123–142 (2005).
2. D. Kereš, N. Katz, D. H. Weinberg, R. Davé, *Mon. Not. R. Astron. Soc.* **363**, 2–28 (2005).
3. X. Fernández *et al.*, *Astrophys. J.* **824**, L1 (2016).
4. A. Wolfe, E. Gawiser, J. Prochaska, *Annu. Rev. Astron. Astrophys.* **43**, 861–918 (2005).
5. J. Prochaska, A. Wolfe, *Astrophys. J.* **487**, 73–95 (1997).
6. M. Rafelski, A. Wolfe, J. Prochaska, M. Neeleman, A. Mendez, *Astrophys. J.* **755**, 89 (2012).
7. M. Pettini, L. Smith, R. Hunstead, D. King, *Astrophys. J.* **426**, 79 (1994).
8. N. Kanekar *et al.*, *Mon. Not. R. Astron. Soc.* **438**, 2131–2166 (2014).
9. P. Møller, S. Warren, S. M. Fall, J. Fynbo, P. Jakobsen, *Astrophys. J.* **574**, 51–58 (2002).
10. J.-K. Krogager *et al.*, *Mon. Not. R. Astron. Soc.* **424**, L1 (2012).
11. M. Neeleman, A. Wolfe, J. Prochaska, M. Rafelski, *Astrophys. J.* **769**, 54 (2013).
12. L. Christensen, P. Møller, J. Fynbo, T. Zafar, *Mon. Not. R. Astron. Soc.* **445**, 225–238 (2014).
13. R. Cen, *Astrophys. J.* **748**, 121 (2012).
14. S. Bird *et al.*, *Mon. Not. R. Astron. Soc.* **445**, 2313–2324 (2014).
15. J. P. U. Fynbo *et al.*, *Mon. Not. R. Astron. Soc.* **408**, 2128–2136 (2010).
16. C. Péroux, N. Bouché, V. Kulkarni, D. York, G. Vladilo, *Mon. Not. R. Astron. Soc.* **410**, 2237–2250 (2011).
17. M. Fumagalli, J. O'Meara, J. Prochaska, M. Rafelski, N. Kanekar, *Mon. Not. R. Astron. Soc.* **446**, 3178–3198 (2015).
18. R. Srianand *et al.*, *Mon. Not. R. Astron. Soc.* **460**, 634–649 (2016).
19. M. Giavalisco *et al.*, *Astrophys. J.* **600**,L93 (2004).
20. S. V. W. Beckwith *et al.*, *Astron. J.* **132**, 1729–1755 (2006).
21. N. A. Grogin *et al.*, *Astrophys. J. Suppl. Ser.* **197**, 35 (2011).
22. Materials and methods are available as supplementary materials.
23. C. Carilli, F. Walter, *Annu. Rev. Astron. Astrophys.* **51**, 105–161 (2013).
24. J. Pineda, W. Langer, T. Velusamy, P. Goldsmith, *Astron. Astrophys.* **554**, A103 (2013).
25. S. Malhotra *et al.*, *Astrophys. J.* **561**, 766–786 (2001).
26. C. C. Steidel, M. Giavalisco, M. Dickinson, K. L. Adelberger, *Astron. J.* **112**, 352 (1996).
27. P. L. Capak *et al.*, *Nature* **522**, 455–458 (2015).
28. I. De Looze *et al.*, *Astron. Astrophys.* **568**, A62 (2014).
29. M. Rafelski *et al.*, *Astrophys. J.* **825**, 87 (2016).
30. A. Font-Ribera *et al.*, *J. Cosmol. Astropart. Phys.* **11**, 059 (2012).
31. K. R. Stewart *et al.*, *Astrophys. J.* **769**, 74 (2013).
32. M. Danovich, A. Dekel, O. Hahn, D. Ceverino, J. Primack, *Mon. Not. R. Astron. Soc.* **449**, 2087–2111 (2015).
33. A. L. Muratov *et al.*, *Mon. Not. R. Astron. Soc.* **454**, 2691–2713 (2015).

ACKNOWLEDGMENTS

Support for this work was provided by the NSF through award SOSPA2-002 from the National Radio Astronomy Observatory (NRAO). M.N. and J.X.P. are partially supported by a grant from the NSF (AST-1412981). N.K. acknowledges support from the Department of Science and Technology via a Swarnajayanti Fellowship (DST/SJF/PSA-01/2012-13), and M.R. was partially supported by a NASA Postdoctoral Program fellowship. ALMA is a partnership of the European Southern Observatory (ESO) (representing its member states), NSF (USA), and the National Institute of Natural Sciences (Japan), together with the National Research Council (Canada), the National Science Council and Academia Sinica Institute of Astronomy and Astrophysics (Taiwan), and Korea Astronomy and Space Science Institute (Republic of Korea), in cooperation with the Republic of Chile. The Joint ALMA Observatory is operated by ESO, Associated Universities Inc. (AUI)/NRAO, and National Astronomical Observatory of Japan. The NRAO is a facility of the NSF operated under cooperative agreement by AUI. Part of the data presented herein were obtained at the W. M. Keck Observatory, which is operated as a scientific partnership among the California Institute of Technology, the University of California, and NASA. The observatory was made possible by the generous financial support of the W. M. Keck Foundation. The data reported in this paper are available though the ALMA archive (https://almascience.nrao.edu/alma-data/archive) with project code ADS/JAO.ALMA#2015.1.01564.S and the Keck Observatory archive (https://koa.ipac.caltech.edu) with program ID U163HR.

SUPPLEMENTARY MATERIALS

www.sciencemag.org/content/355/6331/1285/suppl/DC1
Materials and Methods
Figs. S1 and S2
Tables S1 to S4
References (*34*–*45*)

7 October 2016; accepted 22 February 2017
10.1126/science.aal1737

PEROVSKITE PHYSICS

Extremely efficient internal exciton dissociation through edge states in layered 2D perovskites

J.-C. Blancon,[1] H. Tsai,[1,2] W. Nie,[1] C. C. Stoumpos,[3] L. Pedesseau,[4] C. Katan,[5] M. Kepenekian,[5] C. M. M. Soe,[3] K. Appavoo,[6] M. Y. Sfeir,[6] S. Tretiak,[1] P. M. Ajayan,[2] M. G. Kanatzidis,[3,7] J. Even,[4] J. J. Crochet,[1]* A. D. Mohite[1]*

Understanding and controlling charge and energy flow in state-of-the-art semiconductor quantum wells has enabled high-efficiency optoelectronic devices. Two-dimensional (2D) Ruddlesden-Popper perovskites are solution-processed quantum wells wherein the band gap can be tuned by varying the perovskite-layer thickness, which modulates the effective electron-hole confinement. We report that, counterintuitive to classical quantum-confined systems where photogenerated electrons and holes are strongly bound by Coulomb interactions or excitons, the photophysics of thin films made of Ruddlesden-Popper perovskites with a thickness exceeding two perovskite-crystal units (>1.3 nanometers) is dominated by lower-energy states associated with the local intrinsic electronic structure of the edges of the perovskite layers. These states provide a direct pathway for dissociating excitons into longer-lived free carriers that substantially improve the performance of optoelectronic devices.

Two-dimensional (2D) Ruddlesden-Popper perovskites (RPPs) are a class of quantum well (QW)–like materials described by the formula $A_nA'_{n-1}M_nY_{3n+1}$, where A and A′ are cations, M is metal, and Y is halide; the value of n determines the QW thickness and, as a result, the degree of quantum and dielectric confinement as well as the optical band gap (or color) (*1*–*9*). They have emerged as an alternative to bulk (3D) organic-inorganic (hybrid) perovskites because of their technologically relevant photostability and chemical stability coupled with high-performance optoelectronic devices (*10*–*12*). Compared with 3D perovskites and classical semiconductor-based QWs, RPPs offer tremendous advantages because of the tunability of their optoelectronic properties through both chemical and quantum-mechanical degrees of freedom. For two decades, RPP crystals with $n = 1$ (*5*, *6*, *13*–*15*) have

[1]Los Alamos National Laboratory, Los Alamos, NM 87545, USA. [2]Department of Materials Science and Nanoengineering, Rice University, Houston, TX 77005, USA. [3]Department of Chemistry, Northwestern University, Evanston, IL 60208, USA. [4]Fonctions Optiques pour les Technologies de l'Information (FOTON), Institut National des Sciences Appliquées (INSA) de Rennes, CNRS, UMR 6082, 35708 Rennes, France. [5]Institut des Sciences Chimiques de Rennes (ISCR), Université de Rennes 1, CNRS, UMR 6226, 35042 Rennes, France. [6]Center for Functional Nanomaterials, Brookhaven National Laboratory, Upton, NY 11973, USA. [7]Department of Materials Science and Engineering, Northwestern University, Evanston, IL 60208, USA.
*Corresponding author. Email: jcrochet@lanl.gov (J.J.C.); amohite@lanl.gov (A.D.M.)

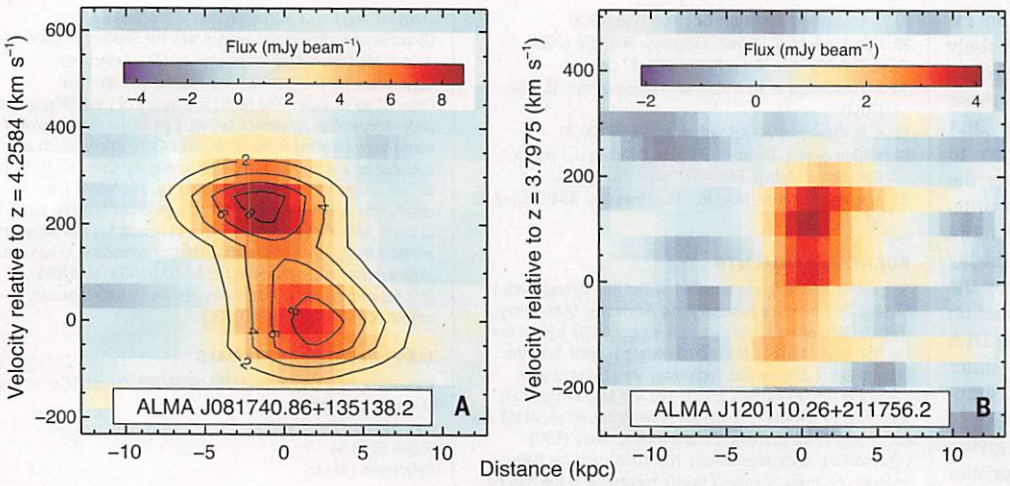

Fig. 3. Position-velocity (*p-v*) diagrams for the [C II] 158-μm emission. (**A** and **B**) Distance is calculated from the center of the [C II] 158-μm emission along the observed major axis of the galaxy (Fig. 1). For ALMA J081740.86+135138.2, a model of a simple uniformly rotating disk is shown in contours (*22*). The agreement between this model and the data suggests that the [C II] 158-μm line originates from a cool gaseous disk. For ALMA J120110.26+211756.2, the [C II] 158-μm emission appears more complicated, albeit at a lower signal-to-noise ratio. mJy, millijansky.

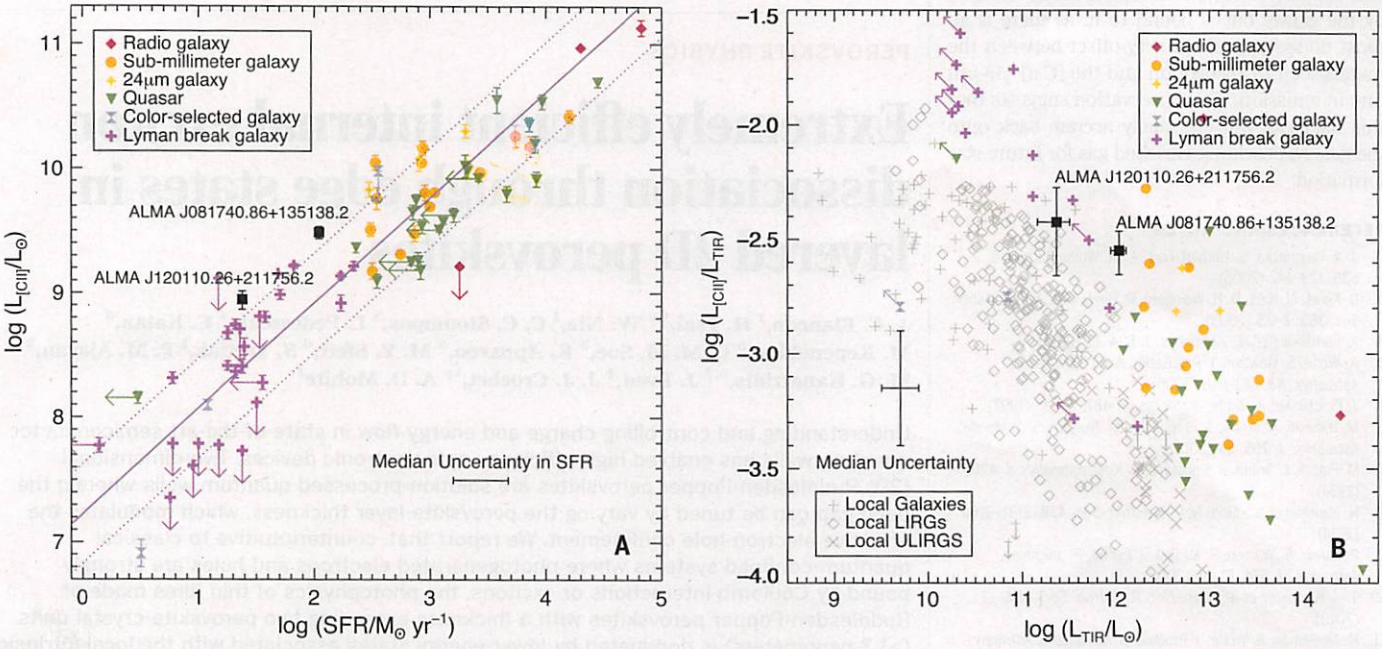

Fig. 4. Comparison of observed properties of the DLA hosts with local and high-redshift galaxies. (**A**) Correlation between the [C II] 158-μm luminosity and star-formation rate (SFR) for a sample of $z > 1$ galaxies categorized by galaxy type (*23*). Also plotted is the correlation for galaxies in the local universe (blue solid line), along with the associated scatter (blue dashed lines) (*28*). (**B**) Ratio of [C II] 158-μm luminosity to total infrared (TIR) luminosity, L_{TIR}, as a function of L_{TIR} for the same sample of $z > 1$ galaxies. Plotted in gray are a sample of local galaxies and local (ultra)luminous infrared galaxies, (U)LIRGs. The high-metallicity, absorption-selected galaxies occupy the same parameter space as moderately star-forming, emission-selected galaxies at similar redshift, suggesting that they have similar characteristics. $L_\odot$, luminosity of the Sun. Error bars indicate 1σ uncertainty.

J081740.86+135138.2 and the dynamical mass estimates of comparable emission-selected galaxies at $z \sim 5$ (*27*). The observed connection between massive LBGs and high-metallicity DLAs supports results from earlier DLA studies at lower redshifts (*9*, *29*) and cross-correlation studies with the Ly-α forest (*30*).

We can use the impact parameter estimates to probe the physical extent of the H I gas around absorption-selected galaxies. The observed impact parameters correspond to physical (proper) distances of 42 and 18 kpc at the DLA redshifts for ALMA J081740.86+135138.2 and ALMA J120110.26+211756.2, respectively. These distances are substantially larger than the extent of the [C II] 158-μm line emission, which extends to ~5 kpc, and indicate that these galaxies have large reservoirs of H I relatively far away from their star-forming regions. The observed distances also require that the emission and absorption lines arise in physically separated gas. Therefore, the absorbing gas must probe either H I gas associated with a satellite galaxy, an enriched neutral outflow from the galaxy, or H I gas in the inner circumgalactic medium/extended disk of the galaxy. The first explanation is disfavored, because the satellite galaxies would need to be metal-enriched and show highly turbulent velocity dispersions of several hundreds of kilometers per second, indicative of massive star-forming systems. However, little star formation is observed, as no [C II] 158-μm emission is seen at the position of the absorber.

The absorbing gas is therefore more likely to reside in the inner gaseous halo of each DLA host galaxy. For the DLA toward SDSS J081740.52+135134.5, the gas is systematically blueshifted along the same direction and with the same magnitude as the rotation of the cool gas disk observed in [C II] 158-μm line emission. This could indicate that the gas

been studied the most with few prototypes of optoelectronic devices (*3*, *16*). Recently, the synthesis of phase-pure (purified to one n value) 2D perovskites with high n values (n = 2 to 5) was achieved (*4*), which led to the demonstration of high-efficiency thin-film solar cells based on RPPs of n = 3 and 4 with technology-relevant stability (*12*). However, there is limited understanding of the fundamental physical properties of phase-pure 2D perovskites of high n value in thin films typically used for optoelectronic applications. Furthermore, the fate of photogenerated electron-hole pairs and the underlying photophysical processes such as charge separation and recombination are unknown.

We investigated photophysical and optoelectronic properties of phase-pure homogenous 2D perovskites and show that in thin films (fig. S1) for n > 2, there exists an intrinsic mechanism for dissociation of the strongly bound electron-hole pairs (excitons) to long-lived free carriers provided by lower-energy states at the edges of the layered perovskites. Moreover, once carriers are trapped in these edge states, they remain protected and do not lose their energy through nonradiative processes and can contribute to photocurrent in a photovoltaic (PV) device or radiatively recombine efficiently as desired for light-emission applications. We validate these findings through PV devices with record efficiencies and two-orders-higher photoluminescence quantum yields (PLQY) using n > 2 layered perovskites.

The crystal structure and evidence for phase purity of the investigated layered 2D perovskite family of $(BA)_2(MA)_{n-1}Pb_nI_{3n+1}$ with n = 1 to 5 are shown in Fig. 1, A and B. In order to understand the origin of the thin-film optical properties, we compared them to those of their exfoliated crystal counterparts prepared by mechanically exfoliating few layers of pristine RPP crystals. The optical absorption and photoluminescence (PL) properties of the thin films and exfoliated crystals are illustrated in Fig. 1, C to F (fig. S1) (*17*), along with bulk $CH_3NH_3PbI_3$ perovskites for comparison.

There was a marked difference in the optical properties of the thin films and exfoliated crystals (Fig. 1, C to H; table S1; and fig. S2) (*17*). In the exfoliated crystals, band-gap absorption and emission increased monotonously from 1.85 to 2.42 eV with decreasing n from 5 to 1 (QW thickness varying from 3.139 to 0.641 nm), which is expected from quantum and dielectric confinement resulting in many-body interactions and large exciton binding energies at room temperature (*5*–*9*, *13*, *18*). This behavior was confirmed by estimating the exciton binding energies as a function of n (figs. S3 and S4) (*17*), which amounts to 380 meV, 270 meV, and an average value of 220 meV for n = 1, n = 2, and n > 2, respectively. These values of exciton binding energy (>200 meV) attest to the robustness of the excitonic states at room temperature in phase-pure RPPs up to n = 5. They are about one order of magnitude larger than the values found in 3D lead halide perovskites (*19*) owing to quantum-confinement effects. Moreover, as compared to lead-salt (LS) materials in which dielectric-confinement effects become dominant, these values are similar to those of LS quantum dots (*20*), LS nanorods (*21*), and LS nanosheets (*22*) for similar confinement lengths (see detailed discussion in section ST1 of the supplementary materials and table S2) (*17*). For n = 3 to 5, the exciton binding energy reached a value of ~200 meV, consistent with a system exhibiting 2D quantum confinement, given negligible enhancement of the Coulomb interactions caused by dielectric confinement (*9*). However, in thin films the optical band gap is in good agreement with that observed for exfoliated crystals for n = 1 and 2 but red shifted by 200 to 300 meV for n = 3 to 5 (Fig. 1G).

We note that the band gap stayed almost constant in thin films with n > 2. Any modification to the pristine 2D perovskite phase during thin-film fabrication has already been excluded (*11*, *12*). Effects such as changes in dielectric environment and differences in crystallinity (*23*, *24*) cannot account for the redshifts observed in RPP thin films for n > 2. The redshifts are also not consistent with electronic impurities at surfaces, interfaces, or boundaries in perovskites where carriers are trapped a few tens of millielectron volts within the band gap (*25*–*28*). Furthermore, optical absorption anisotropy measurements (fig. S5) rule out effects from different orientations of the perovskite layers with respect to light polarization in both thin films and exfoliated crystals (*17*).

We further studied the microscopic origin of the low-energy band gap in thin films for n > 2 by confocal spatial mapping (~1-μm resolution) of the PL on a representative n = 3 exfoliated crystal (Fig. 2A). Although the majority of the basal plane of exfoliated crystal yields spatially homogeneous PL at its band-gap energy (2.010 eV), appreciable PL emission was observed from the edges of the exfoliated crystal at 1.680 eV. Figure 2B

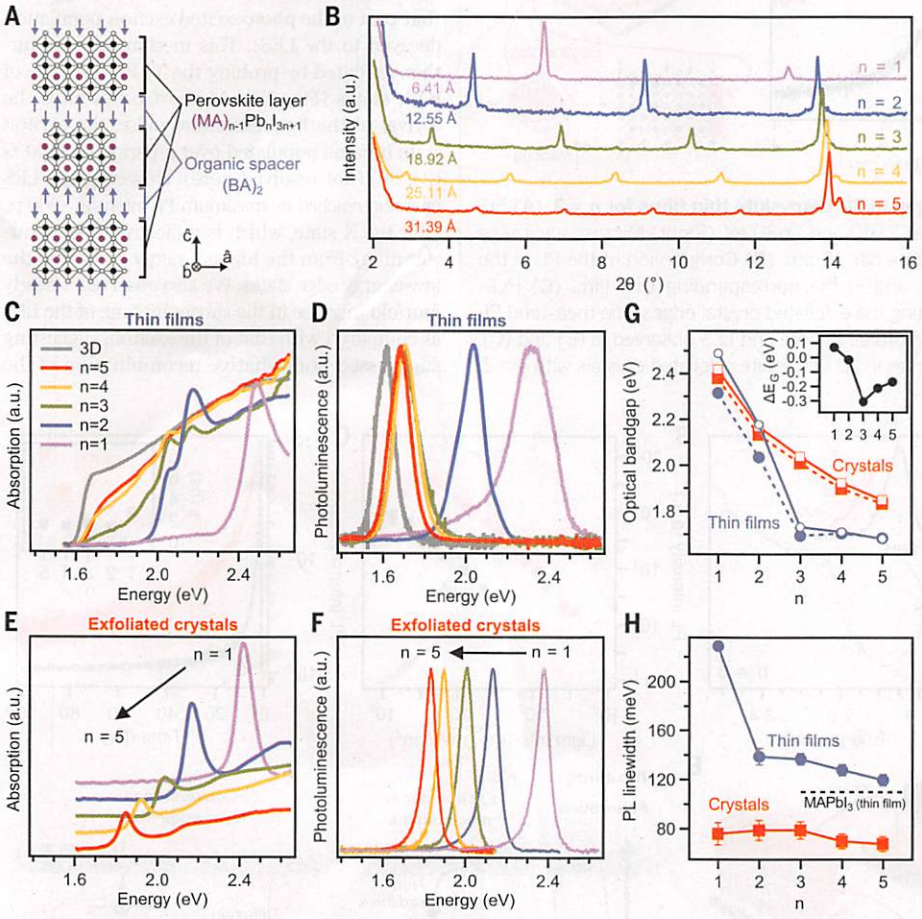

Fig. 1. Evidence of phase purity of the RPPs (n = 1 to 5) and comparison of optical properties of thin films and exfoliated crystals. (**A**) Schematics of the QW-like crystal structure showing perovskite layers in the plane ($\hat{a}, \hat{b}$) sandwiched between organic spacing layers. (**B**) Phase purity established by monitoring the position and number of the low-angle peaks in x-ray diffraction patterns for each n value. a.u., arbitrary units. Absorption and PL of the thin films (**C** and **D**) and exfoliated crystals (**E** and **F**). (**G**) Optical band gap derived from absorption (open symbols) and PL (filled symbols) as a function of n. (Inset) Shift of the optical band gap in thin films with respect to exfoliated crystals (from absorption). (**H**) PL linewidth versus n, showing inhomogeneous broadening in thin films as compared with that of exfoliated crystals.

illustrates the PL spectra of the exfoliated crystal, edges of the exfoliated crystal, and corresponding thin film. The spectra collected at the crystal edges contain PL peaks observed in both the thin film and exfoliated crystal, which indicates a common origin of the PL from states associated with the edges of the exfoliated crystal [labeled as layer-edge states (LESs)] and the PL at low energy in thin films for $n > 2$. Similar results were obtained in the case of $n = 4$ and 5 RPP exfoliated crystals (fig. S6) (*17*), whereas the LES emission was absent when $n = 1$ or 2.

We probed the spectral origin of the emitting states observed above using PL excitation (PLE) spectroscopy and time-resolved PL (TRPL). The PLE measurements were performed near the edges of the exfoliated crystal in Fig. 2A and revealed both the main exciton emission (labeled X state) at 2.010 eV and the LES at 1.680 eV. We monitored the PL intensity at the LES energy while sweeping the light-excitation energy between 1.800 and 2.900 eV (Fig. 2C). The PLE showed a clear peak at the position of the exciton (2.010 ± 0.007 eV) but no direct absorption into the LES was observed in the exfoliated crystal (PLE was negligible below 1.900 eV). The spectrum exhibited two high-energy features at ~2.110 and 2.200 eV, associated with excited excitonic states and band-to-band absorption, which yielded an exciton binding energy of 200 meV, in agreement with our absorption measurements (Fig. 1E).

These results and the comparable PL intensity of both the X state and LES features suggested that part of the photoexcited exciton population decayed to the LESs. This mechanism was further validated by probing the TRPL response of both states (Fig. 2D). At short times after the arrival of the light-excitation pulse, the exciton state became populated over a period of ~100 fs (*25*, *29*) (not resolved here). However, the LES emission reached its maximum PL intensity ~200 ps after the X state, which is indicative of slow carrier filling from the higher-energy exciton to the low-energy edge states. We also observed a nearly fourfold increase in the carrier lifetime of the LES as compared with that of the exciton, suggesting suppressed nonradiative recombination of the

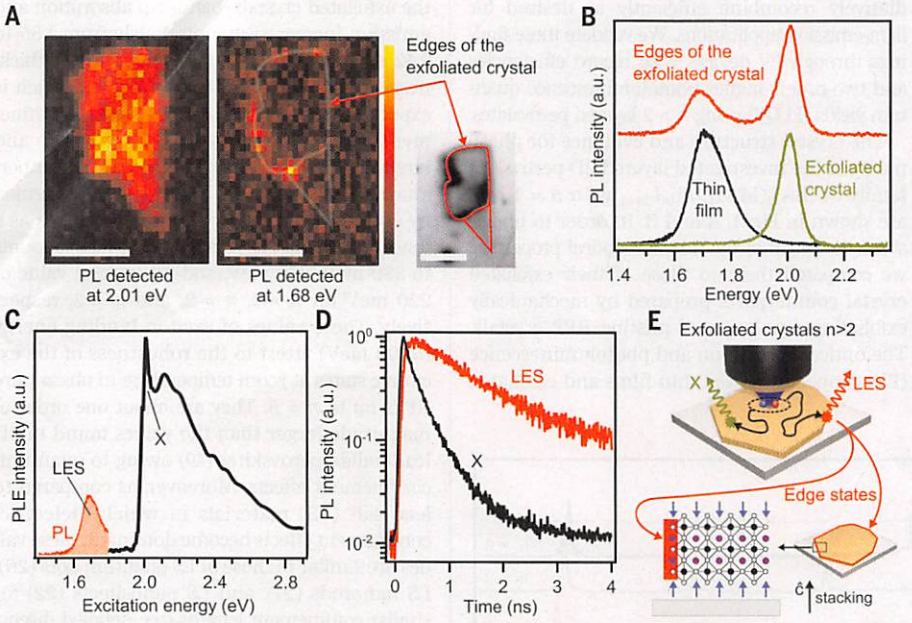

Fig. 2. Microscopic origin of the low-energy band gap in 2D perovskite thin films for $n = 3$. (**A**) PL-intensity map of a single exfoliated crystal, probed at 2.010 and 1.680 eV. (Right) Microscopy image showing the layer edges of the exfoliated crystal. Scale bar, 10 μm. (**B**) Comparison of the PL in the exfoliated crystal, at the exfoliated-crystal edges, and in the corresponding thin film. (**C**) PLE-integrated signal of the LES, measured by locally exciting the exfoliated-crystal edges. The measured PL profile of the LES is also plotted. (**D**) TRPL of the PL features X state and LES observed in (B) and (C). (**E**) Schematics of the photoabsorption and PL processes in 2D perovskite exfoliated crystals with $n > 2$.

Fig. 3. Optical absorption and emission mechanisms in thin films of 2D perovskites. (**A**) Thin film $n = 3$ absorption (green), PL at photoexcitation 100 mW/cm^2 (black) and 10^6 mW/cm^2 (red). (**B**) I_0 dependence of the integrated PL. Dashed lines are fits to the data. (**C**) TRPL in the thin films $n = 3$. (Inset) Corresponding lifetimes (τ) of the X states and LESs as a function of the n value. Excitation at ~100 mW/cm^2. (**D**) Schematics of the photoabsorption and PL processes in a 2D perovskite thin film with $n > 2$. In contrast to exfoliated crystals, thin-film perovskite layers are preferentially oriented normal to the substrate (fig. S10) (*12*, *17*), therefore, excitation light probes numerous amounts of LESs. (**E**) Summary of the main photoemission mechanisms in thin films. The diffusion length was estimated from fig. S13 (*17*). VB and CB stand for valence and conduction bands, respectively.

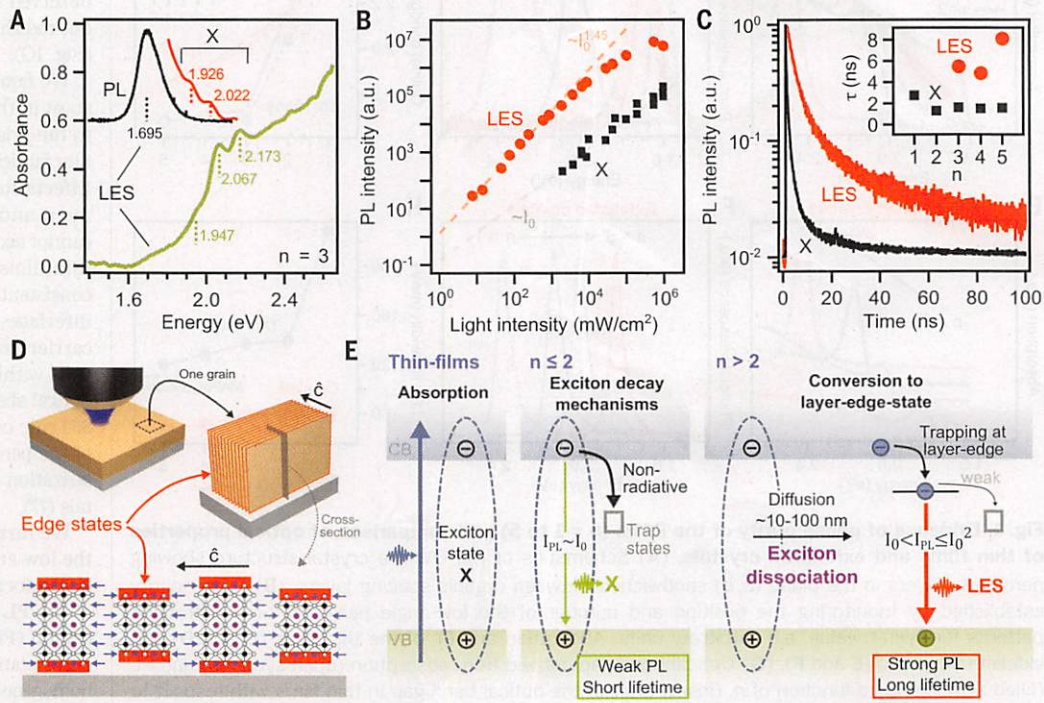

localized carriers. Figure 2E schematically summarizes the photoemission mechanisms in 2D perovskites. The photoexcited exciton diffuses in the perovskite layer, emitting a photon at the exciton energy (geminate radiative recombination), or can be quenched through nonradiative recombination. However, these measurements elucidate that, in 2D perovskites with $n > 2$, a part of the photogenerated exciton population travels to the edges of the crystal within its diffusion time and then undergoes an internal conversion to a LES and efficiently emits photons at a lower energy than the main exciton.

We gained further insight into the physical origin of the optical transitions (Fig. 1, C and D) by analyzing the absorption and photoemission properties of thin films. Figure 3A describes the transitions in thin films with $n = 3$ (see fig. S7 for the other n values) (*17*). The absorption spectrum exhibits resonances at 1.947 ± 0.005, 2.067 ± 0.006, and 2.173 ± 0.006 eV, which are very close in energy to the main exciton state in exfoliated crystals (2.039 eV). These features were also observed in the PL spectra at relatively high light-excitation intensity I_0 (Fig. 3A, inset), i.e., after saturating the lower-energy LES population. The excitonic nature of these optical resonances was confirmed through (i) linear dependence of the integrated PL signal with respect to I_0 (Fig. 3B, black) and (ii) the negative temperature dependence of their peak energy (figs. S8 and S9) (*5*, *6*, *17*). On the other hand, the main PL peak at 1.695 ± 0.015 eV (Fig. 3A, inset) corresponds to the LES peak observed in exfoliated crystals (Fig. 2B). In sharp contrast to exfoliated crystals (Fig. 2), the PL was dominated by the LES peak, and a broad absorption feature around 1.73 eV (Fig. 3A) accounts for direct absorption into this LES and related minibands. These features are a direct consequence of both the light sampling across numerous LESs in thin films (Fig. 3D) because of preferential orientation of perovskite layers normal to the substrate (fig. S10) (*12*, *17*), small grain sizes typically of the order of 200 to 400 nm (fig. S11) (*12*, *17*), and the relaxation of optical-transition selection rules in imperfect crystals.

We also observed that the PL signal associated with the LES varied nonlinearly with the light-excitation intensity between $I_0^{1.30}$ and $I_0^{1.45}$ (Fig. 3B and fig. S7) (*17*). This signal corresponds to a mixed bimolecular and monomolecular recombination of photoexcited carriers (*27*), thus implying a partial dissociation of excitons to free carrier–like entities as the excitonic states convert (or dissociate) to the LESs. This conclusion is also consistent with the smooth rise of the absorption at the optical band gap in comparison to the sharp excitonic features observed in exfoliated crystals (Fig. 1, C and E). Moreover, the energy of the LESs varied with temperature as 0.21 meV/K (fig. S12) (*17*), which has been attributed in 3D perovskites to the thermal expansion of the lattice where free carriers dominate (*30*). On the contrary, the RPPs with $n \leq 2$ that do not exhibit the LES showed negligible or negative temperature dependence of their optical resonances (fig. S8) (*17*), consistent with classical excitonic theory (*5*, *6*).

All of these measurements establish a different physical origin and behavior of the excitonic and LES features and validate that the main band-gap optical transition in RPP thin films with $n > 2$ originates from the intrinsic electronic structure associated with the edges of the 2D perovskite layers (see discussion in section ST2 in the supplementary materials on the possible causes of LES formation) (*17*). Based on our observations, the primary mechanism that emerges in thin films is trapping of the free carriers after exciton dissociation to a deep electronic state located at layer edges. This model is compatible with both the higher PL efficiency and the longer lifetime of the LESs as compared with those of the higher-energy X states (Fig. 3, B and C). These results imply that, once the carriers are localized at LESs, they are protected from nonradiative decay mechanisms such as electron-phonon coupling (*31*, *32*) or electronic impurities (*25*). These key mechanisms of the photoemission in RPPs are captured in Fig. 3E (fig. S13), where, after photogeneration of excitons (left), they can either decay through classical processes (dominant for $n \leq 2$, middle) or dissociate to free carriers potentially trapped at the LESs (dominant for $n > 2$, right). The process involving intrinsic dissociation of the primary photogenerated excitons to free carrier–like states that exist lower in energy in a single-component material is nonintuitive and not observed in any classical quantum-confined material system.

Motivated by the observed internal exciton dissociation from a part of the higher-energy excitonic states to the LESs that protect the carriers over an appreciably longer time scale, we fabricated high-efficiency PV cells with RPPs and measured their current-voltage (*J-V*) characteristics and power conversion efficiency (PCE) (Fig. 4, A and B). We observed a sharp break in the current density and PCE from <2% for n = 1 and 2 to >12% for $n > 2$. Assuming comparable charge-transport properties for all RPPs, the performances of PV cells for $n > 2$ are impacted by the presence of the LES as (i) it extends the absorption from the visible to the near infrared and (ii) it contributes to internal exciton dissociation to free carrier–like entities that can be more readily collected by the built-in field in a PV device. This was confirmed by measuring the external quantum efficiency (EQE) spectra (Fig. 4C), which showed about fivefold enhancement in collection efficiency in PV cells using RPPs with $n > 2$ as compared to RPPs with n = 1 and 2. Furthermore, the free carriers that converge to the LESs remain protected, thus exhibiting long recombination carrier lifetimes resulting in a much higher probability for efficient PL (Fig. 4D and fig. S14) (*17*), which has tremendous implications for high-efficiency light-emitting devices using RPPs with $n > 2$. The variations of the PL efficiency in thin films and of the solar cell efficiency (*33*) between RPPs with n = 3, 4, and 5 were possibly due to small variations of the crystal crystallinity and ordering (*12*) and/or light out-coupling and photon-recycling effects (*34*). These results not only pave the path forward for the rational design of high-efficiency optoelectronic devices with solution-processed layered 2D perovskite-based materials, but they are also relevant to a large group of materials with edges and surface states.

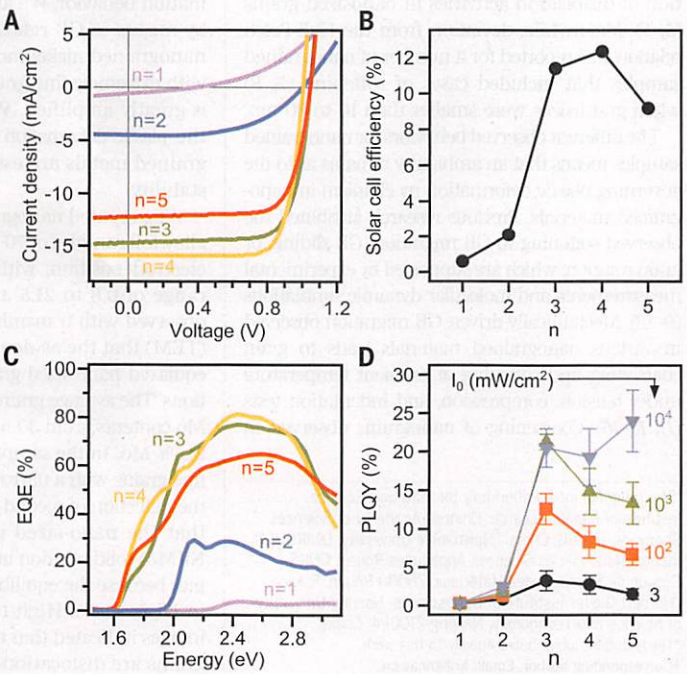

Fig. 4. Figures of merit of thin-film devices for light-harvesting and solid-state emission. (**A**) *J-V* characteristics measured under AM1.5 illumination. (**B**) Power-conversion efficiency as a function of 2D perovskite n value (QW thickness). (**C**) EQE for the PV devices in (A). (**D**) PLQY in thin films as a function of n value for several light-excitation intensities.

REFERENCES AND NOTES

1. S. N. Ruddlesden, P. Popper, *Acta Crystallogr.* **10**, 538–539 (1957).
2. S. N. Ruddlesden, P. Popper, *Acta Crystallogr.* **11**, 54–55 (1958).
3. C. R. Kagan, D. B. Mitzi, C. D. Dimitrakopoulos, *Science* **286**, 945–947 (1999).
4. C. C. Stoumpos *et al.*, *Chem. Mater.* **28**, 2852–2867 (2016).

5. T. Ishihara, J. Takahashi, T. Goto, *Phys. Rev. B Condens. Matter* **42**, 11099–11107 (1990).
6. N. Kitazawa, M. Aono, Y. Watanabe, *J. Phys. Chem. Solids* **72**, 1467–1471 (2011).
7. J. Even, L. Pedesseau, C. Katan, *ChemPhysChem* **15**, 3733–3741 (2014).
8. D. Sapori, M. Kepenekian, L. Pedesseau, C. Katan, J. Even, *Nanoscale* **8**, 6369–6378 (2016).
9. L. Pedesseau *et al.*, *ACS Nano* **10**, 9776–9786 (2016).
10. I. C. Smith, E. T. Hoke, D. Solis-Ibarra, M. D. McGehee, H. I. Karunadasa, *Angew. Chem. Int. Ed.* **53**, 11232–11235 (2014).
11. D. H. Cao, C. C. Stoumpos, O. K. Farha, J. T. Hupp, M. G. Kanatzidis, *J. Am. Chem. Soc.* **137**, 7843–7850 (2015).
12. H. Tsai *et al.*, *Nature* **536**, 312–316 (2016).
13. K. Tanaka, T. Kondo, *Sci. Technol. Adv. Mater.* **4**, 599–604 (2003).
14. K. Tanaka *et al.*, *Jpn. J. Appl. Phys.* **44**, 5923–5932 (2005).
15. K. Gauthron *et al.*, *Opt. Express* **18**, 5912–5919 (2010).
16. D. B. Mitzi, K. Chondroudis, C. R. Kagan, *IBM J. Res. Develop.* **45**, 29–45 (2001).
17. Materials and methods are available as supplementary materials.
18. O. Yaffe *et al.*, *Phys. Rev. B* **92**, 045414 (2015).
19. L. M. Herz, *Annu. Rev. Phys. Chem.* **67**, 65–89 (2016).
20. J. Jasieniak, M. Califano, S. E. Watkins, *ACS Nano* **5**, 5888–5902 (2011).
21. A. C. Bartnik, A. L. Efros, W.-K. Koh, C. B. Murray, F. W. Wise, *Phys. Rev. B* **82**, 195313 (2010).
22. J. Yang, F. W. Wise, *J. Phys. Chem. C* **119**, 26809–26816 (2015).
23. J.-C. Blancon *et al.*, *Nat. Commun.* **4**, 2542 (2013).
24. Y. Lin *et al.*, *Nano Lett.* **14**, 5569–5576 (2014).
25. X. Wu *et al.*, *J. Am. Chem. Soc.* **137**, 2089–2096 (2015).
26. W. Nie *et al.*, *Science* **347**, 522–525 (2015).
27. J.-C. Blancon *et al.*, *Adv. Funct. Mater.* **26**, 4283–4292 (2016).
28. D. W. de Quilettes *et al.*, *Science* **348**, 683–686 (2015).
29. K. Abdel-Baki *et al.*, *J. Appl. Phys.* **119**, 064301 (2016).
30. H. Wang, L. Whittaker-Brooks, G. R. Fleming, *J. Phys. Chem. C* **119**, 19590–19595 (2015).
31. Z. Guo, X. Wu, T. Zhu, X. Zhu, L. Huang, *ACS Nano* **10**, 9992–9998 (2016).
32. D. B. Straus *et al.*, *J. Am. Chem. Soc.* **138**, 13798–13801 (2016).
33. O. D. Miller, E. Yablonovitch, S. R. Kurtz, *IEEE J. Photovolt.* **2**, 303–311 (2012).
34. J. M. Richter *et al.*, *Nat. Commun.* **7**, 13941 (2016).

ACKNOWLEDGMENTS

The work at Los Alamos National Laboratory (LANL) was supported by the LANL Laboratory Directed Research and Development (LDRD) program (J.-C.B., W.N., S.T., and A.D.M.) and was partially performed at the Center for Nonlinear Studies. The work was conducted, in part, at the Center for Integrated Nanotechnologies (CINT), a U.S. Department of Energy (DOE), Office of Science user facility. Work at Northwestern University was supported by grant SC0012541 from the U.S. DOE, Office of Science. The work in France was supported by Cellule Energie du CNRS (SOLHYBTRANS Project) and University of Rennes 1 (Action Incitative, Défis Scientifique Emergents 2015). This research used resources of the Center for Functional Nanomaterials, which is a U.S. DOE Office of Science facility, at Brookhaven National Laboratory under contract no. DE-SC0012704. J.-C.B., A.D.M., and J.J.C. conceived the idea, designed the experiments, and wrote the manuscript. H.T. and W.N. fabricated thin films and performed all device measurements and analysis. J.E., C.K., and S.T. analyzed the data and performed Heyd-Scuseria-Ernzerhof screened-exchange hybrid functional calculations with support from M.K. and L.P. and provided insight into the mechanisms. M.G.K., C.C.S., and C.M.M.S. developed the chemistry for the synthesis of phase-pure crystals and provided insight into the chemical origin of the edge states. M.S. and K.A. performed several complementary measurements to provide insight into the mechanisms and to validate the observed findings. P.M.A. provided insights into the origin of edge states. All authors contributed to this work, read the manuscript, and agree to its contents, and all data are reported in the main text and supplementary materials.

SUPPLEMENTARY MATERIALS

www.sciencemag.org/content/355/6331/1288/suppl/DC1
Materials and Methods
Supplementary Text
Figs. S1 to S14
Tables S1 and S2
References (*35*–*40*)

17 November 2016; accepted 22 February 2017
Published online 9 March 2017
10.1126/science.aal4211

METALLURGY

Grain boundary stability governs hardening and softening in extremely fine nanograined metals

J. Hu,[1]* Y. N. Shi,[1]* X. Sauvage,[2] G. Sha,[3] K. Lu[1,3]†

Conventional metals become harder with decreasing grain sizes, following the classical Hall-Petch relationship. However, this relationship fails and softening occurs at some grain sizes in the nanometer regime for some alloys. In this study, we discovered that plastic deformation mechanism of extremely fine nanograined metals and their hardness are adjustable through tailoring grain boundary (GB) stability. The electrodeposited nanograined nickel-molybdenum (Ni–Mo) samples become softened for grain sizes below 10 nanometers because of GB-mediated processes. With GB stabilization through relaxation and Mo segregation, ultrahigh hardness is achieved in the nanograined samples with a plastic deformation mechanism dominated by generation of extended partial dislocations. Grain boundary stability provides an alternative dimension, in addition to grain size, for producing novel nanograined metals with extraordinary properties.

The strength or hardness of conventional polycrystalline metals increases with decreasing grain sizes following the classical Hall-Petch relationship (*1*, *2*); the increase in strength is reversely proportional to the square root of grain size. This relationship is established with the strengthening mechanism based on dislocation pileups at grain boundaries (GBs), which hinder dislocation motion. Plastic deformation becomes more difficult at smaller grains with higher density of GBs. Grain-size reduction into the nanometer scale makes dislocation pileup difficult, raising into question continued hardening. Experimental observations are mixed, with continuous hardening detected in some metals with grain sizes as small as 10 nm (*3*, *4*), which agrees with the experimental identification of dislocation activities in nanosized grains (*5*, *6*). Meanwhile, deviation from the Hall-Petch relation was reported for a number of nanograined samples that included cases of softening (*7*, *8*) when grain sizes were smaller than 10 to 30 nm.

The different observed behaviors for nanograined samples means that an ambiguity remains as to the governing plastic deformation mechanism in nanograined materials. Previous research attributed the observed softening to GB migration, GB sliding, or grain rotation, which are supported by experimental measurements and molecular dynamic simulations (*9*–*12*). Mechanically driven GB migration observed in various nanograined materials leads to grain coarsening and softening at ambient temperature under tension, compression, and indentation tests (*11*, *13*–*15*). Coarsening of nanograins observed in thin-film samples under plastic deformation was attributed to grain rotations (*9*). These studies regard the numerous GBs in nanograined materials not only as barriers to slip transmission, as in conventional coarse-grained materials, but also the primary facilitators for plastic deformation (*16*).

The kinetic process of the GB-mediated deformation depends on the nature of GBs. Compared with the low-energy boundaries such as twin boundary or low-angle GBs, the conventional high-angle GBs exhibit lower thermal and mechanical stability (*16*). Nevertheless, high-angle GBs can be effectively stabilized through GB relaxation (*17*), GB segregation of solute atoms (*18*, *19*), or both processes. Hence, by tailoring GB stability, we expected adjustments to the GB-mediated processes and the corresponding plastic deformation behavior. We aimed to tailor GB stability by means of GB relaxation and segregation in nanograined nickel-molybdenum (Ni–Mo) alloys with extremely fine grains in which the GB effect is greatly amplified. We present evidence that the plastic deformation and hardness of the nanograined metals are essentially governed by GB stability.

We prepared nanograined pure Ni and Ni–Mo alloy foil samples of 70 μm thickness by using DC electrodeposition, with Mo concentrations in a range of 0.8 to 21.5 atomic % (at %) (*20*). We observed with transmission electron microscopy (TEM) that the as-deposited samples consist of equiaxed nano-sized grains with random orientations. The average grain size decreases with higher Mo contents, from 30 nm in pure Ni to 3.4 nm for 21.5% Mo. In the samples, we observed extremely fine grains with a narrow size distribution without the detection of second phase (Fig. 1). This implies that the nano-sized grains are supersaturated Ni(Mo) solid solution in the high Mo-content samples because the equilibrium solid solubility of Mo in Ni is ~14%. High-resolution TEM (HRTEM) images indicated that the randomly oriented tiny grains are dislocation-free crystals (Fig. 1C). In

[1]Shenyang National Laboratory for Materials Science, Institute of Metal Research, Chinese Academy of Sciences, Shenyang 110016, China. [2]Normandie University, UNIROUEN, Institut National des Sciences Appliquées Rouen, CNRS, Groupe de Physique des Matériaux, 76000 Rouen, France. [3]Herbert Gleiter Institute of Nanoscience, Nanjing University of Science and Technology, Nanjing 210094, China.
*These authors contributed equally to this work.
†Corresponding author. Email: lu@imr.ac.cn